Engineering Analysis with Boundary Elements 143 (2022) 568–578

Contents lists available at ScienceDirect

Engineering Analysis with Boundary Elements

journal homepage: www.elsevier.com/locate/enganabound

A multi-domain BEM based on dual interpolation boundary face method for 3D elasticity problem

Pengfei Chai, Jianming Zhang *, Rongxiong Xiao, Rui He, WeiCheng Lin

State Key Laboratory of Advanced Design and Manufacturing for Vehicle Body, College of Mechanical and Vehicle Engineering, Hunan University, Changsha 410082, China

ARTICLE INFO

Keywords:
Multi-domain method
Short edge and small chamfers
Dual interpolation boundary face method
Hermite-type approximation

ABSTRACT

The dual interpolation boundary face method with Hermite-type moving-least-squares approximation (DiBFM-HMLS), presented recently, has certain advantages in simulating the discontinuous fields. Based on the DiBFM-HMLS and the matrix condensation technique, we proposed a multi-domain method for 3D elasticity problems in this paper. This method ensures an accurate interpolation for the multi-domain models with short edges or small chamfers. In the multi-domain DiBFM-HMLS, the virtual points in each subdomain, not as collocation points in the boundary integral equation (BIE), are eliminated by the HMLS approximation separately. Then, only the interfacial source points are reserved by the matrix condensation technique. The node-to-node interfacial condition in previous research is unemployed; instead of the former, a node-to-element format is constructed based on the moving-least-squares approximation (MLS). This mapping scheme possesses the potential for free mesh in the interface. Several numerical examples are used to reflect these advantages mentioned above.

1. Introduction

Multi-domain boundary element method (MDBEM) is proven to be an excellent method [1–4] in promoting the computational efficiency of the single-domain boundary element method (SDBEM). MDBEM refers to a tearing and interconnecting routine in which the targeted domain is divided into subdomains, and then equilibrium and continuum conditions are enforced to couple subdomains. In recent decades, MDBEM has received significant development. To obtain a more favorable linear system, some methods based on Galerkin discretization (e.g., Chen, Tianzhi et al. [5], Layton et al. [6], and Kallivokas et al. [7]) were proposed to form a partial or complete symmetric coefficient matrix, which provided convenience for condensation or direct solution. After that, a set of studies on multi-domain problems with the fast multipole method (FMM) were implemented to accelerate the solution and reduce the computational complexity (e.g., U. Langer et al. [8], G. OF et al. [9], Huang et al. [10], and Zhang et al. [11]). Besides the FMM, the multi-domain methods based on the fast iterative linear least square technique [12–14] emerged as a parallel method with its FMM counterparts. Moreover, other efforts were devoted to reducing the ultimate linear systems by the matrix condensation technique (e.g., Gao et al. [15], Peng et al. [16], and Zheng et al. [17]). These researches circumvented the discontinuity (e.g., tractions or flux) at the geometric corner by resorting to the nonconforming elements. Nevertheless, inaccurate interpolation or hyper-singular integral will be brought into the analysis for geometric structures with short edges or small chamfers.

In order to tackle the problems at the geometric and physical corners, Zhang et al. [18–20] developed the dual interpolation boundary face method with the moving least-squares approximation (DiBFM-MLS). The dual interpolation elements in DiBFM-MLS (see Fig. 1(d)) cover the deficiencies of the conforming (see Fig. 1(a) and (b)) and nonconforming elements (see Fig. 1(c)) in treating the discontinuous fields. The virtual points in dual interpolation elements are not regarded as collocation points in BIE; thus, to obtain solvable linear equations, the relationship matrices constructed by MLS are used to condense these points. Unfortunately, the interpolation functions of MLS are built on the parametric coordinates, making them unfit for structures with small feature sizes. To obtain an accurate interpolation in geometric structures with short edges or small chamfers, recently, we proposed a dual interpolation boundary face method with Hermite-type moving-least-squares approximation (DiBFM-HMLS) [21,22]. In this method, the normal equations are established on the Cartesian coordinate rather than the parameter space, which guarantees an accurate interpolation of the physical variables in the small feature sizes.

* Corresponding author.
E-mail address: zhangjm@hnu.edu.cn (J. Zhang).

https://doi.org/10.1016/j.enganabound.2022.07.003
Received 17 May 2022; Received in revised form 21 June 2022; Accepted 5 July 2022
Available online 21 July 2022

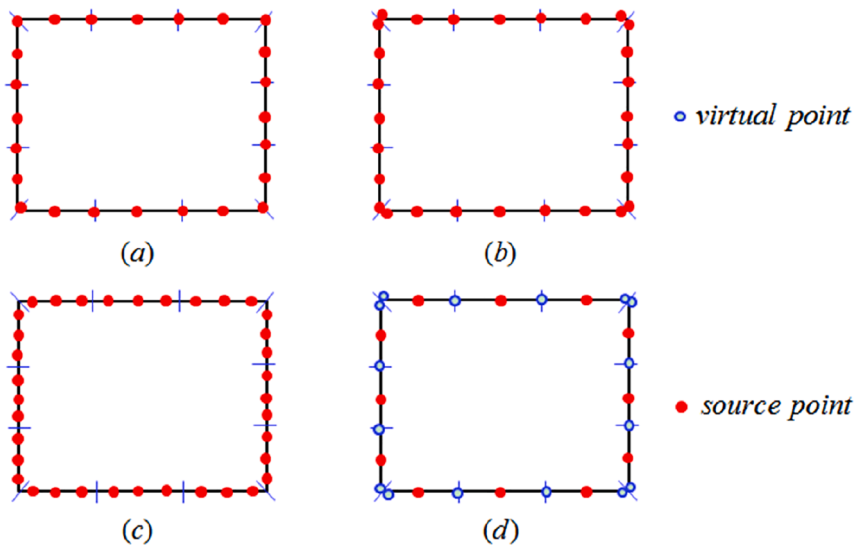

Fig. 1. Quadratic elements: (a) continuous elements, (b) continuous elements with multiple-node method, (c) discontinuous elements, and (d) dual interpolation elements.

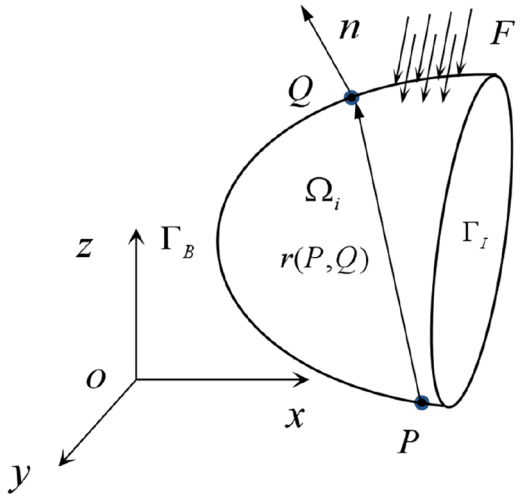

Fig. 2. A 3D elastic domainΩwith interface.

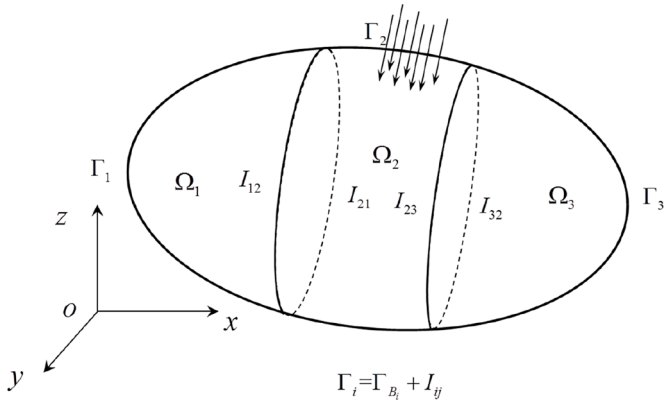

Fig. 3. 3D Multi-domain model.

Based on the above advantages, a multi-domain method combining the DiBFM-HMLS and the matrix condensation technique is addressed for 3D elasticity problems. The DiBFM-HMLS is employed to discretize

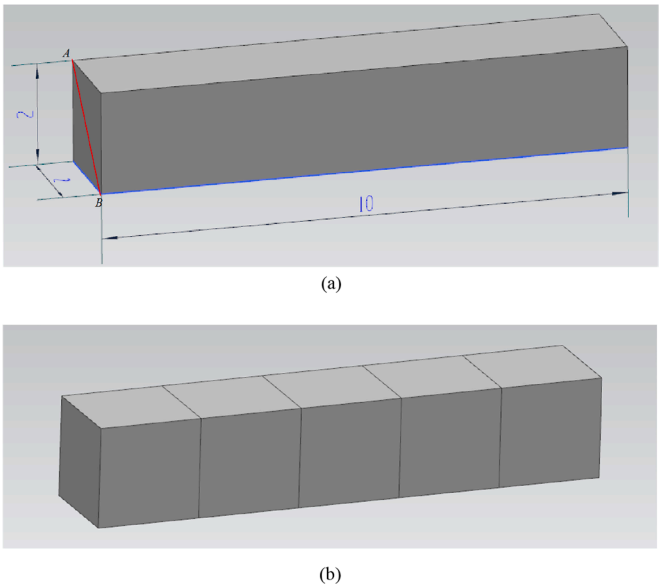

Fig. 4. Model for bar (a) single domain and (b) multi-domain.

the BIE of each subdomain, and the matrix condensation technique [15–17] is used to obtain the linear equations concerning the interfacial source points. Compared with its reduction counterparts, the blocked-sparse coefficient matrix is still available, and the corner problem can be dealt with by DiBFM-HMLS naturally. Furthermore, the node-to-node interfacial condition is dismissed; and a node-to-element projective format, building on the MLS approximation [18–20], is present; this mapping scheme can provide convenience for free meshing in contact problems.

An outline of the paper is to proceed as follows: a brief review of the BEM for elasticity problem and the discretization of BIE by DiBFM-HMLS are stated in Section 2. The proposed multi-domain method based on DiBFM-HMLS is presented in Section 3. Several example applications are illustrated in Section 4 to verify our multi-domain algorithm. Some conclusions and discussions on deficiency and future development are drawn in Section 5.

Table 1
Relative error and CPU time of single-domain method and multi-domain method.

Multi-domain DiBFM				Single-domain DiBFM			
NE	NS	*Err_Mises*	*time*(s)	NE	NS	*Err_Mises*	*time*(s)
1920	1920	8.50E-07	391	1854	1854	1.80E-06	324
3000	3000	7.20E-07	667	3072	3072	2.50E-07	924
5070	5070	9.90E-08	1506	5070	5070	2.40E-07	2760
12,000	12,000	3.70E-08	9972	10,736	10,736	1.80E-07	13,542

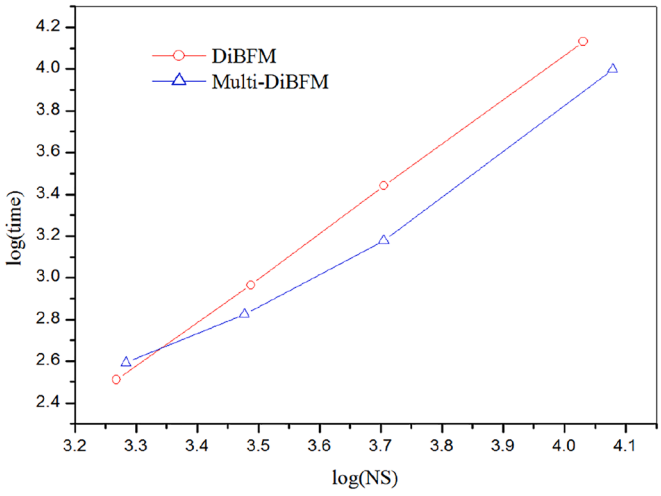

Fig. 5. Comparison of the computational efficiency between single-domain DiBFM and multi-domain DiBFM.

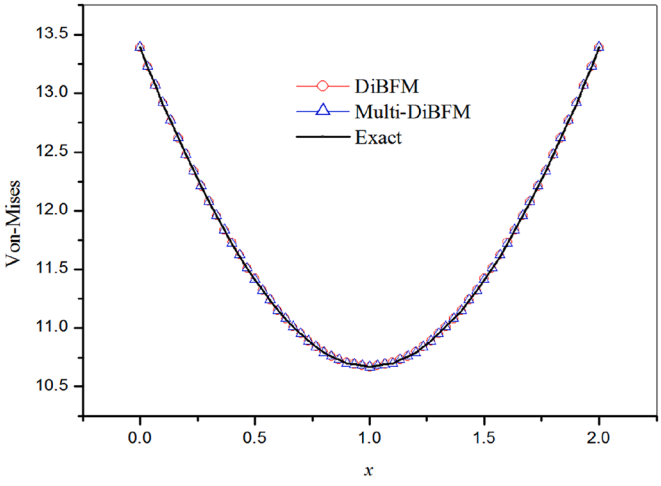

Fig. 6. Comparison of Von-Mises stress along with line AB.

2. DiBFM-HMLS for 3D elasticity problems

2.1. Boundary integral equation

For 3D elastic domain Ω (see Fig. 2) with boundary Γ ($\Gamma = \Gamma_B + \Gamma_I$), Γ_I is the interface with the other domain. The boundary integral equation (BIE) can be written as:

$$c_{kl}(P)u_l(P) = \int_\Gamma U^*_{kl}(P,Q)t_l(Q)d\Gamma(Q) - \int_\Gamma T^*_{kl}(P,Q)u_l(Q)d\Gamma(Q)\ \ (k,l=1,2,3), \tag{1}$$

in which *k*, *l* are the direction components in the Cartesian coordinate system, *P* represents the source point, *Q* denotes the field point, coefficient $c_{kl}(P) = 1/2\delta_{kl}$ when *P* locate on the smooth surface, and$U^*_{kl}(P,Q)$ and$T^*_{kl}(P,Q)$ are the fundamental solutions [23] which are the response in *Q* along with *ι-th* direction when a unite load acts on *P* in *k-th* direction. For 3D elasticity problems with plane strain case,$U^*_{kl}(P,Q)$ and$T^*_{kl}(P,Q)$ are given by:

$$U^*_{kl}(P,Q) = \frac{1}{16\pi\mu(1-\nu)r(P,Q)}\left[(3-4\nu)\delta_{kl} + r_{,k}(P,Q)r_{,l}(P,Q)\right], \tag{2}$$

$$T^*_{kl}(P,Q) = \frac{1}{8\pi(1-\nu)r^2(P,Q)}\left\{\begin{array}{l}\dfrac{\partial r(P,Q)}{\partial n(Q)}\left[(1-2\nu)\delta_{kl} + 3r_{,k}(P,Q)r_{,l}(P,Q)\right] \\ -(1-2\nu)\left[r_{,k}(P,Q)n_l(Q) - r_{,l}(P,Q)n_k(Q)\right]\end{array}\right\}, \tag{3}$$

where *r*(P, Q) is the distance between points *P* and *Q*, μ and *ν* are the shear modulus and the Poisson's ratio, respectively.$\delta_{kl} = \begin{cases}1, & k=l\\ 0, & k\neq l\end{cases}$ is the Kronecker delta. n_k and n_l are the component of the unit outward normal *n*, respectively.

2.2. Discretization of the BIE

Different from the conventional boundary element method (CBIE), in DiBFM, the BIE is discretized by dual interpolation elements, and the discretization form of Eq. (1) is given by

$$\sum_{e=1}^{NE}\left[\sum_{\alpha=1}^{n\alpha} h^{ss}_{kl}\left(P^s_m, Q^s_\alpha\right)u^s_l(Q_\alpha) + \sum_{\beta=1}^{n\beta} h^{sv}_{kl}\left(P^s_m, Q^v_\beta\right)u^v_l(Q_\beta)\right] = \sum_{e=1}^{NE}\left[\sum_{\alpha=1}^{n\alpha} g^{ss}_{kl}\left(P^s_m, Q^s_\alpha\right)t^s_l(Q_\alpha) + \sum_{\beta=1}^{n\beta} g^{sv}_{kl}\left(P^s_m, Q^v_\beta\right)t^v_l(Q_\beta)\right],\ \ m = 1,2,\ldots,NS, \tag{4}$$

with

$$h^{ss}_{kl}(P_m,Q) = \int_{\Gamma_e} T^*_{kl}(P_m,Q)N^s_\alpha(Q)d\Gamma_e(Q) + \frac{1}{2}\delta_{kl}\delta^m_\alpha, \tag{5}$$

$$h^{sv}_{kl}(P_m,Q) = \int_{\Gamma_e} T^*_{kl}(P_m,Q)N^v_\beta(Q)d\Gamma_e(Q), \tag{6}$$

$$g^{ss}_{kl}(P_m,Q) = \int_{\Gamma_e} U^*_{kl}(P_m,Q)N^s_\alpha(Q)d\Gamma_e(Q), \tag{7}$$

$$g^{sv}_{kl}(P_m,Q) = \int_{\Gamma_e} U^*_{kl}(P_m,Q)N^v_\beta(Q)d\Gamma_e(Q), \tag{8}$$

and

$$\delta^m_\alpha = \begin{cases}1, & \text{if the m}^{\text{th}}\text{ source node is the }\alpha^{\text{th}}\text{ source node in }e^{\text{th}}\text{ element}\\ 0\end{cases}, \tag{9}$$

where NE, *nα*, and *nβ* are the numbers of elements, source nodes, and virtual nodes.$u^s_l(Q_\alpha)$ and$t^s_l(Q_\alpha)$ are the displacement and the traction along with *ι-th* direction of the *α-th* source point in *e-th* dual interpolation element.$u^v_l(Q_\beta)$ and$t^v_l(Q_\beta)$ are the displacement and the traction of the *β-th* virtual point in the same element.$N^s_\alpha(Q)$ and$N^s_\beta(Q)$ represents the

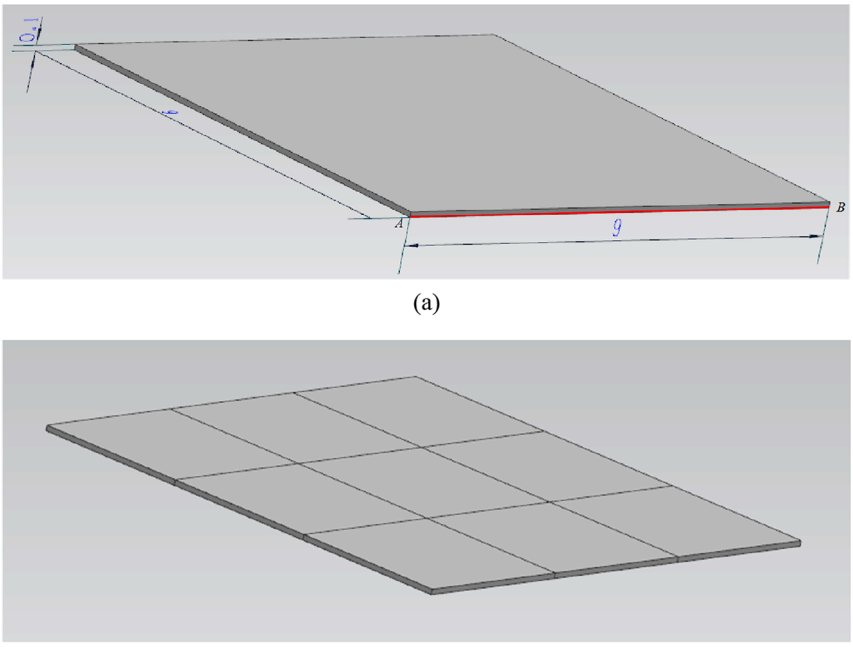

(a)

(b)

Fig. 7. Model for thin plate (a) single domain and (b) multi-domain.

Table 2
Relative error and CPU time of single-domain method and multi-domain method.

Multi-domain DiBFM				Single-domain DiBFM			
NE	NS	*Err_Mises*	*time*(s)	NE	NS	*Err_Mises*	*time*(s)
1524	1524	1.80E-04	281	1532	1532	1.60E-05	245
3120	3120	7.50E-05	797	3112	3112	8.41E-06	997
4770	4770	5.23E-05	1860	4772	4772	4.20E-06	2362
11,274	11,274	3.80E-05	3980	10,722	10,722	3.60E-06	13,606

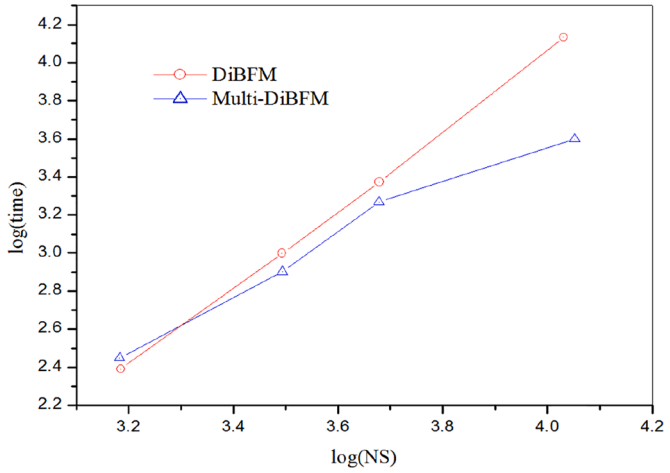

Fig. 8. Comparison of the computational efficiency between single-domain DiBFM and multi-domain DiBFM.

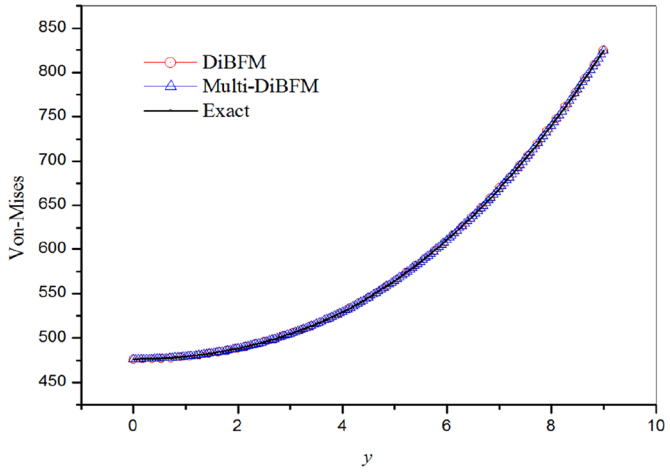

Fig. 9. Comparison of Von-Mises stress along with line AB.

shape function of the α-*th* source point and the β-*th* virtual point in a dual interpolation element.

Eq. (4) can be written as an index form:

$$\mathbf{H}_{kl}^{ss}\mathbf{u}_l^s + \mathbf{H}_{kl}^{sv}\mathbf{u}_l^v = \mathbf{G}_{kl}^{ss}\mathbf{t}_l^s + \mathbf{G}_{kl}^{sv}\mathbf{t}_l^v \tag{10}$$

where $k, l = 1, 2, 3.\mathbf{u}_l^s,\mathbf{u}_l^v,\mathbf{t}_l^s$, and$\mathbf{t}_l^v$ are displacement and traction vectors along with ι-*th* direction corresponding to source points and virtual points.$\mathbf{H}_{kl}^{ss}(3NS \times 3NS),\mathbf{G}_{kl}^{ss}(3NS \times 3NS),\mathbf{H}_{kl}^{sv}(3NS \times 3NV)$, and$\mathbf{G}_{kl}^{sv}(3NS \times 3NV)$ are coefficient matrices (NS and NV are the number of source and virtual points respectively) corresponding tou$_l^s$,$\mathbf{t}_l^s$,$\mathbf{u}_l^v$, and$\mathbf{t}_l^v$. Here,$\mathbf{H}_{kl}^{sv}$ and$\mathbf{G}_{kl}^{sv}$ are not square anymore because the virtual points are not regarded as collocation points in BIE.

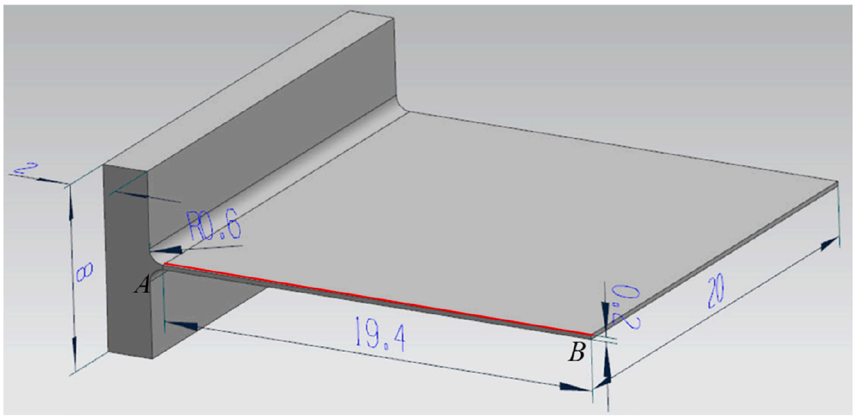

(a)

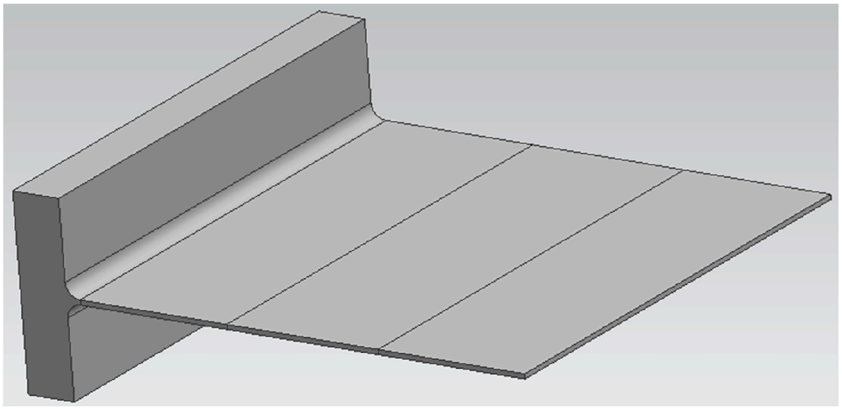

(b)

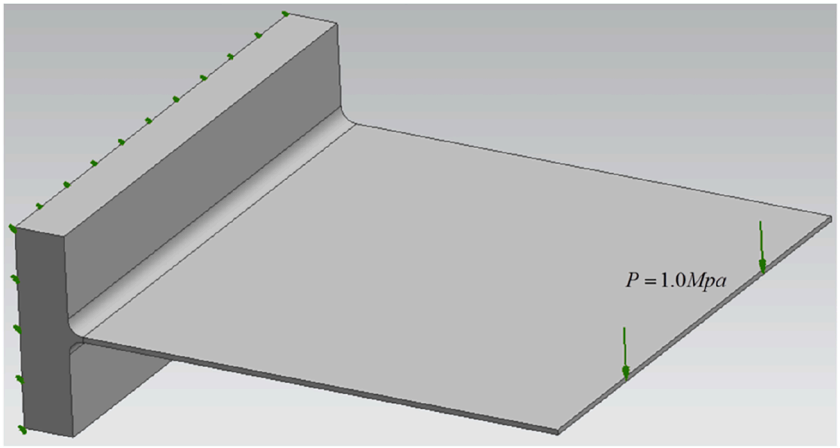

(c)

Fig. 10. Model for cantilever slab (a) single domain (b) multi-domain, and (c) boundary conditions.

2.3. Condensation of degrees of freedom of virtual nodes

To get a solvable system of linear equations, the second layer interpolation by HMLS is used to condense the virtual points.$\mathbf{u}_k^v$ and$\mathbf{t}_k^v$ are separated into different parts according to the boundary conditions, which can be written as the following form:

$$\mathbf{u}_k^v = \overline{\mathbf{u}}_k^{v_\Gamma} + \widehat{\mathbf{u}}_k^{v_\Gamma}, \tag{11}$$

$$\mathbf{t}_k^v = \overline{\mathbf{t}}_k^{v_\Gamma} + \widehat{\mathbf{t}}_k^{v_\Gamma}, \tag{12}$$

$\overline{\mathbf{u}}_k^{v_\Gamma}$,$\overline{\mathbf{t}}_k^{v_\Gamma}$, and$\widehat{\mathbf{u}}_k^{v_\Gamma}$,$\widehat{\mathbf{t}}_k^{v_\Gamma}$, are the known and unknown vectors of the virtual nodes. The unknown variables$\widehat{\mathbf{u}}_k^{v_\Gamma}$ and$\widehat{\mathbf{t}}_k^{v_\Gamma}$ can be approximated by HMLS as follows:

$$\widehat{u}_k^{v_\Gamma} = \mathbf{\Phi}^{vs}_{u_k u_l}\mathbf{u}_l^s + \mathbf{\Phi}^{vs}_{u_k t_l}\mathbf{t}_l^s, \tag{13}$$

$$\widehat{t}_k^{v_\Gamma} = \mathbf{\Phi}^{vs}_{t_k u_l}\mathbf{u}_l^s + \mathbf{\Phi}^{vs}_{t_k t_l}\mathbf{t}_l^s, \tag{14}$$

where$\mathbf{\Phi}^{vs}_{u_k u_l}$,$\mathbf{\Phi}^{vs}_{u_k t_l}$,$\mathbf{\Phi}^{vs}_{t_k u_l}$, and$\mathbf{\Phi}^{vs}_{t_k t_l}$ are shape function matrices [22] obtained by the HMLS approximation.

According to Eqs. (11)-(14) and the boundary conditions, the matrix form of Eq. (10) can be obtained by

Table 3
Von-Mises and CPU time of multi-domain method, single domain method, and FEM.

Multi-domain DiBFM	NE	7368	9254	11,644	14,973
	NS	7368	9254	11,644	14,973
	Max_Mises (Mpa)	448.08	532.83	568.87	574.02
	time(s)	2747	5808	9076	20,302
Single-domain DiBFM	NE	7552	9121	11,215	14,706
	NS	7552	9121	11,215	14,706
	Max_Mises (Mpa)	713.68	589.74	573.62	586.42
	time(s)	5742	8542	13,186	23,588
FEM	NE	17,661	47,312	208,078	1075,194
	NN	30,605	78,517	316,981	725,942
	Max_Mises (Mpa)	550.9	567.9	592.7	572.2

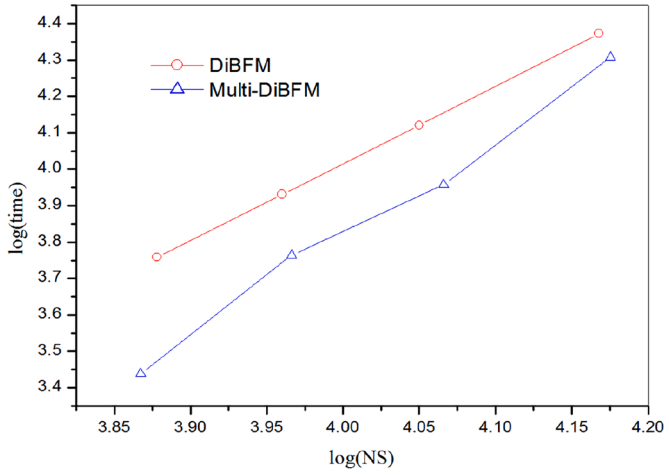

Fig. 11. Comparison of the computational efficiency between single-domain DiBFM and multi-domain DiBFM.

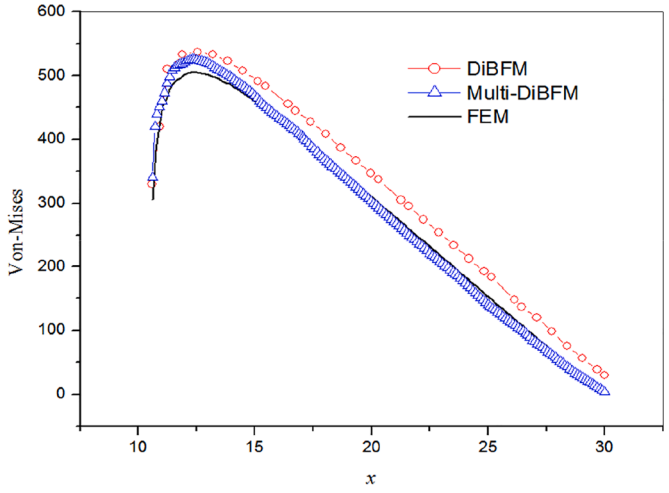

Fig. 12. Comparison of Von-Mises stress along with line AB.

$$\begin{bmatrix} \widehat{\mathbf{M}}_{kl}^{s_B s_B} & \widehat{\mathbf{H}}_{kl}^{s_B s_I} & -\widehat{\mathbf{G}}_{kl}^{s_B s_I} \\ \widehat{\mathbf{M}}_{kl}^{s_I s_B} & \widehat{\mathbf{H}}_{kl}^{s_I s_I} & -\widehat{\mathbf{G}}_{kl}^{s_I s_I} \end{bmatrix} \begin{Bmatrix} \widehat{\mathbf{x}}_l^{s_B} \\ \widehat{\mathbf{u}}_l^{s_I} \\ \widehat{\mathbf{t}}_l^{s_I} \end{Bmatrix} = \begin{bmatrix} \overline{\mathbf{M}}_{kl}^{s_B s_B} & \overline{\mathbf{M}}_{kl}^{s_B v_B} \\ \overline{\mathbf{M}}_{kl}^{s_I s_B} & \overline{\mathbf{M}}_{kl}^{s_I v_B} \end{bmatrix} \begin{Bmatrix} \overline{\mathbf{x}}_l^{s_B} \\ \overline{\mathbf{x}}_l^{v_B} \end{Bmatrix}, \tag{15}$$

in which, $\overline{\mathbf{x}}_l^{s_B}$ and $\overline{\mathbf{x}}_l^{v_B}$ are the known variables corresponding to the source and virtual nodes on the boundary along with the *l-th* direction, and $\widehat{\mathbf{x}}_l^{s_B}, \widehat{\mathbf{u}}_l^{s_I}$, and $\widehat{\mathbf{t}}_l^{s_I}$ are unknown variables on boundary and interface. While $\overline{\mathbf{M}}_{kl}^{ss}, \overline{\mathbf{H}}_{kl}^{ss}$, and $\overline{\mathbf{G}}_{kl}^{ss}$ are the coefficient matrices corresponding to the known variables, and $\widehat{\mathbf{M}}_{kl}^{ss}, \widehat{\mathbf{H}}_{kl}^{ss}$, and $\widehat{\mathbf{G}}_{kl}^{ss}$ correspond to unknown parts.

For Dirichlet boundary condition:

$$\begin{aligned} &\overline{\mathbf{M}}_{kl}^{ss} = -\overline{\mathbf{H}}_{kl}^{ss}, \quad \widehat{\mathbf{M}}_{kl}^{ss} = -\widehat{\mathbf{G}}_{kl}^{ss}, \\ &\widehat{\mathbf{M}}_{kl}^{ss} = -\left(\mathbf{G}_{kl}^{sv}\boldsymbol{\Phi}_{t_k t_l}^{vs} - \mathbf{H}_{kl}^{sv}\boldsymbol{\Phi}_{u_k t_l}^{vs}\right), \end{aligned} \tag{16}$$

and Neumman boundary condition:

$$\begin{aligned} &\overline{\mathbf{M}}_{kl}^{ss} = \overline{\mathbf{G}}_{kl}^{ss}, \quad \widehat{\mathbf{M}}_{kl}^{ss} = -\widehat{\mathbf{G}}_{kl}^{ss}, \\ &\widehat{\mathbf{M}}_{kl}^{ss} = \mathbf{H}_{kl}^{ss} + \mathbf{H}_{kl}^{sv}\boldsymbol{\Phi}_{u_k u_l}^{vs} - \mathbf{G}_{kl}^{sv}\boldsymbol{\Phi}_{t_k u_l}^{vs}, \end{aligned} \tag{17}$$

3. Multi-domain method based on DiBFM-HMLS

Assuming that an elastic domain Ω is surrounded by boundary $\Gamma=\partial\Omega$, and the single domain is decomposed into N non-overlapping sub-domains $\Omega_i (i = 1,2\ldots\mathrm{N}$, see Fig. 3), and the boundary is split into several pieces $\Gamma_i=\partial\Omega_i (i = 1,2\ldots\mathrm{N})$. Γ_i consists of the boundary part Γ_{B_i} and the interface part $I_{ij} (i \neq j,\ j = 1,2\cdots\mathrm{N})$, respectively.

3.1. Condensation of degrees of freedom on the boundary

The BIE and its discretization form (Eq. (15)) are constructed for each subdomain $\Omega_i (i = 1,2\ldots\mathrm{N})$ in MDBEM.

$$\begin{bmatrix} \widehat{\mathbf{M}}_{kl}^{s_{B_i} s_{B_i}} & \widehat{\mathbf{H}}_{u_k u_l}^{s_{B_i} s_{I_{ij}}} & -\widehat{\mathbf{G}}_{t_k t_l}^{s_{B_i} s_{I_{ij}}} \\ \widehat{\mathbf{M}}_{kl}^{s_{I_{ij}} s_{B_i}} & \widehat{\mathbf{H}}_{u_k u_l}^{s_{I_{ij}} s_{I_{ij}}} & -\widehat{\mathbf{G}}_{t_k t_l}^{s_{I_{ij}} s_{I_{ij}}} \end{bmatrix} \begin{Bmatrix} \widehat{\mathbf{x}}_l^{s_{B_i}} \\ \widehat{\mathbf{u}}_l^{s_{I_{ij}}} \\ \widehat{\mathbf{t}}_l^{s_{I_{ij}}} \end{Bmatrix} = \begin{bmatrix} \overline{\mathbf{M}}_{kl}^{s_{B_i} s_{B_i}} & \overline{\mathbf{M}}_{kl}^{s_{B_i} v_{B_i}} \\ \overline{\mathbf{M}}_{kl}^{s_{I_{ij}} s_{B_i}} & \overline{\mathbf{M}}_{kl}^{s_{I_{ij}} v_{B_i}} \end{bmatrix} \begin{Bmatrix} \overline{\mathbf{x}}_l^{s_{B_i}} \\ \overline{\mathbf{x}}_l^{v_{B_i}} \end{Bmatrix}, \tag{18}$$

The condensation technique [15] is used to eliminate the degrees of freedom on the boundary in Eq. (18). A system of linear equations concerning unknown interfacial variables of source points can be given as

$$\mathbf{A}_{u_k u_l}^{s_{I_{ij}} s_{I_{ij}}} \widehat{\mathbf{u}}_l^{s_{I_{ij}}} - \mathbf{A}_{t_k t_l}^{s_{I_{ij}} s_{I_{ij}}} \widehat{\mathbf{t}}_l^{s_{I_{ij}}} = \overline{\mathbf{b}}_k^{s_{I_{ij}}}, \tag{19}$$

where

$$\begin{aligned} \mathbf{A}_{u_k u_l}^{s_{I_{ij}} s_{I_{ij}}} &= \widehat{\mathbf{H}}_{u_k u_l}^{s_{B_i} s_{I_{ij}}} - \widehat{\mathbf{M}}_{kl}^{s_{I_{ij}} s_{B_i}} \left(\widehat{\mathbf{M}}_{kl}^{s_{B_i} s_{B_i}}\right)^{-1} \widehat{\mathbf{H}}_{u_k u_l}^{s_{B_i} s_{I_{ij}}}, \\ \mathbf{A}_{t_k t_l}^{s_{I_{ij}} s_{I_{ij}}} &= \widehat{\mathbf{G}}_{t_k t_l}^{s_{I_{ij}} s_{I_{ij}}} - \widehat{\mathbf{M}}_{kl}^{s_{I_{ij}} s_{B_i}} \left(\widehat{\mathbf{M}}_{kl}^{s_{B_i} s_{B_i}}\right)^{-1} - \widehat{\mathbf{G}}_{t_k t_l}^{s_{B_i} s_{I_{ij}}}, \\ \overline{\mathbf{b}}_k^{s_{I_{ij}}} &= \begin{bmatrix} \overline{\mathbf{M}}_{kl}^{s_{I_{ij}} s_{B_i}} & \overline{\mathbf{M}}_{kl}^{s_{I_{ij}} v_{B_i}} \end{bmatrix} \begin{Bmatrix} \overline{\mathbf{x}}_l^{s_{B_i}} \\ \overline{\mathbf{x}}_l^{v_{B_i}} \end{Bmatrix} - \widehat{\mathbf{M}}_{kl}^{s_{I_{ij}} s_{B_i}} \left(\widehat{\mathbf{M}}_{kl}^{s_{B_i} s_{B_i}}\right)^{-1} \begin{bmatrix} \overline{\mathbf{M}}_{kl}^{s_{B_i} s_{B_i}} & \overline{\mathbf{M}}_{kl}^{s_{B_i} v_{B_i}} \end{bmatrix} \begin{Bmatrix} \overline{\mathbf{x}}_l^{s_{B_i}} \\ \overline{\mathbf{x}}_l^{v_{B_i}} \end{Bmatrix}, \end{aligned} \tag{20}$$

multiply Eq. (19) by $\mathbf{A}_{t_k t_l}^{s_{I_{ij}} s_{I_{ij}}{}^{-1}}$, we can get

$$\mathbf{A}_{u_k u_l}^{s_{I_{ij}} s_{I_{ij}}} \mathbf{u}_l^{s_{I_{ij}}} - \mathbf{t}_l^{s_{I_{ij}}} = \mathbf{b}_k^{s_{I_{ij}}}, \ (i = 1,2\cdots N, j = 1,2\cdots N,\ i \neq j), \tag{21}$$

the same derivation processes for other subdomain Ω_m $(m < n, m \neq i, n \neq i)$ are repeated.

3.2. Assemble of the coefficient matrix for interface

Additional conditions for unknown variables on the interfaces are

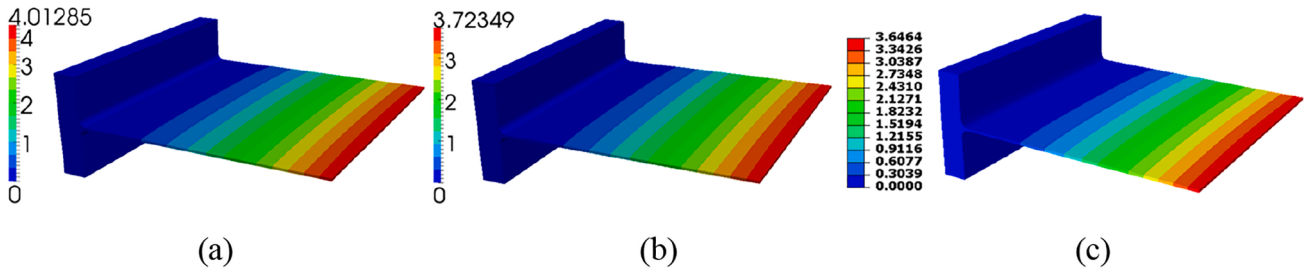

Fig. 13. Contour plots for displacement (a) single-domain DiBFM with 14,706 source nodes, (b) multi-domain DiBFM with 14,973 source nodes, and (c) FEM with 1075,194 nodes.

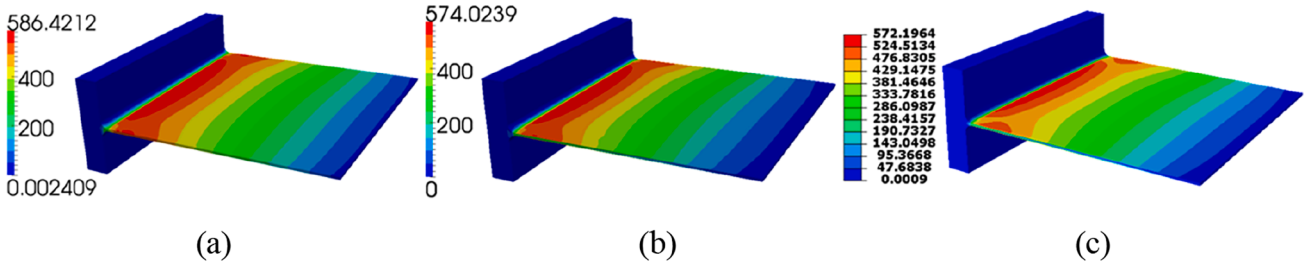

Fig. 14. Contour plots for Von-Mises (a) single-domain DiBFM with 14,706 source nodes, (b) multi-domain DiBFM with 14,973 source nodes, and (c) FEM with 1075,194 nodes.

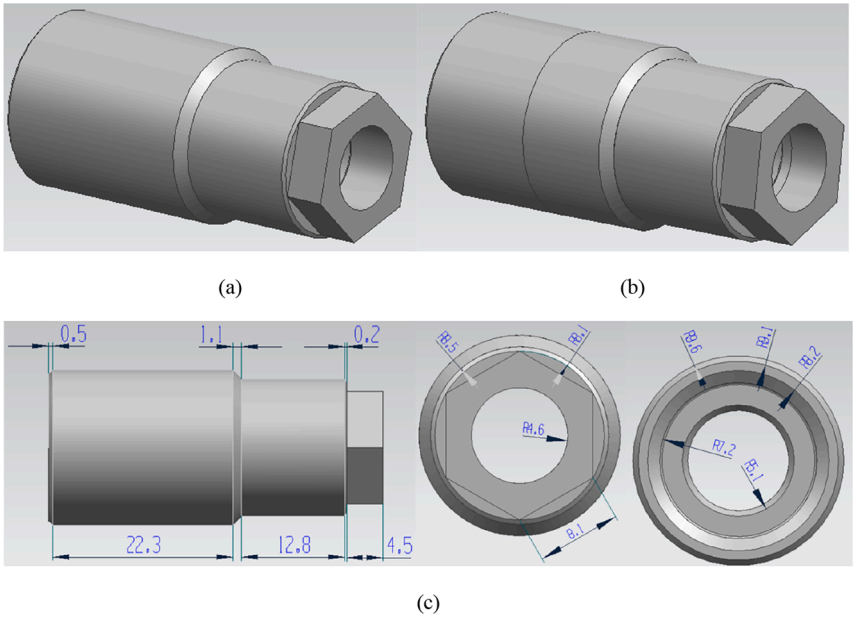

Fig. 15. Model for thin plate (a) single domain (b) multi-domain, and (c) geometric dimension.

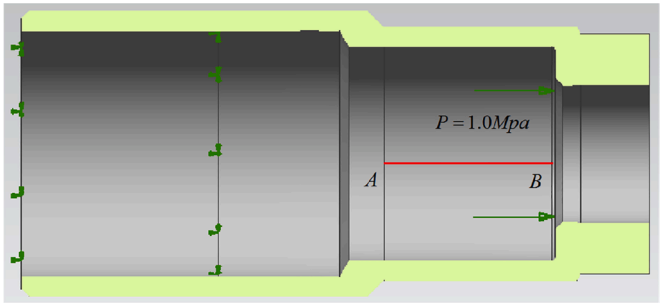

Fig. 16. Boundary condition for nozzle cap nut.

required to bond adjacent subdomains. The node-element constraints on interface pair$I_{ij} - I_{ji}$for elasticity problem are given by

$$\mathbf{u}_k^{s_{I_{ij}}} = \mathbf{F}^{ss}_{I_{ij}I_{ji}}\mathbf{u}_k^{s_{I_{ji}}} + \mathbf{F}^{sv}_{I_{ij}I_{ji}}\mathbf{u}_k^{v_{I_{ji}}}, \tag{22}$$

$$\mathbf{t}_k^{s_{I_{ji}}} = -\mathbf{F}^{ss}_{I_{ji}I_{ij}}\mathbf{t}_k^{s_{I_{ij}}} - \mathbf{F}^{sv}_{I_{ji}I_{ij}}\mathbf{t}_k^{v_{I_{ij}}}, \tag{23}$$

$$\mathbf{F}^{ss}_{I_{ij}I_{ji}} = \mathbf{N}^{ss}_{I_{ij}I_{ji}}, \quad \mathbf{F}^{sv}_{I_{ij}I_{ji}} = \mathbf{N}^{sv}_{I_{ij}I_{ji}}\boldsymbol{\Theta}^{vs}_{I_{ji}I_{ji}}, \tag{24}$$

where$\mathbf{F}^{ss}_{I_{ij}I_{ji}}$ and$\mathbf{F}^{sv}_{I_{ij}I_{ji}}$ are projection matrices from interface I_{ij} to interface I_{ji}. On the contrary,$\mathbf{F}^{ss}_{I_{ji}I_{ij}}$ and$\mathbf{F}^{sv}_{I_{ji}I_{ij}}$ are matrices from I_{ji} toI_{ij}.$\mathbf{N}^{ss}_{I_{ij}I_{ji}}$ and$\mathbf{N}^{sv}_{I_{ij}I_{ji}}$ are matrices consisting of shape functions of the dual interpolation elements

Table 4
Von-Mises and CPU time of multi-domain method, single domain method, and FEM.

Multi-domain DiBFM	NE	6788	9472	11,777	13,614
	NS	6788	9472	11,777	13,614
	Max_Mises (Mpa)	2.59	3.10	2.98	3.01
	time(s)	1672	3798	6950	18,493
Single-domain DiBFM	NE	6780	9473	11,534	13,416
	NS	6780	9473	11,534	13,416
	Max_Mises (Mpa)	2.99	2.95	3.11	3.15
	time(s)	9069	15,263	18,382	26,274
FEM	NE	74,285	119,049	190,324	825,148
	NN	119,027	185,612	292,536	120,6467
	Max_Mises (Mpa)	3.11	3.12	3.19	3.20

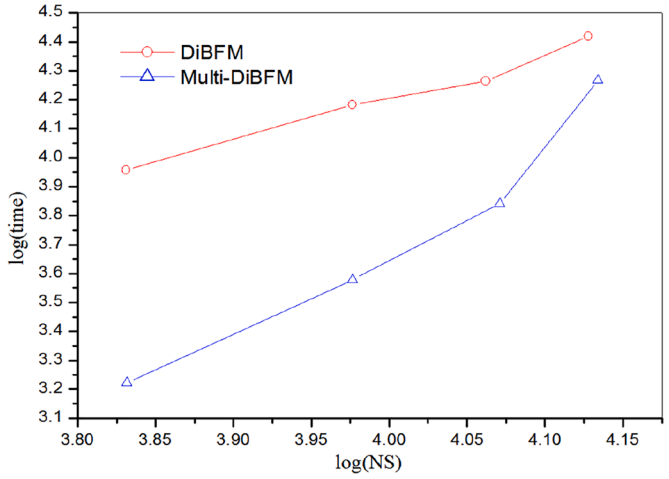

Fig. 17. Comparison of the computational efficiency between single-domain DiBFM and multi-domain DiBFM.

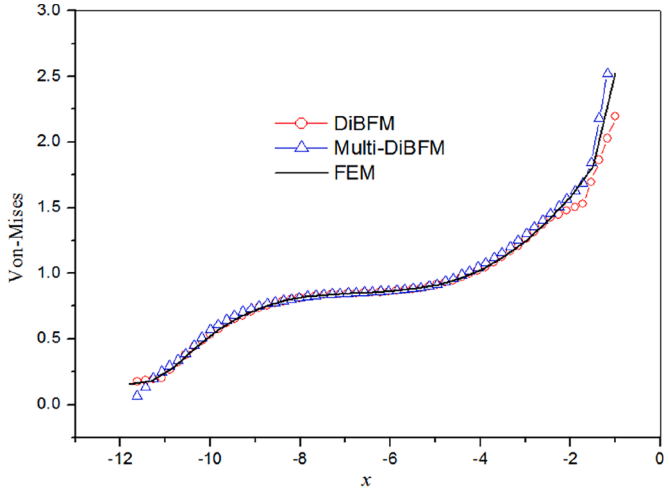

Fig. 18. Comparison of Von-Mises stress along with line AB.

on interface I_{ji}. $\boldsymbol{\Theta}^{vs}_{I_{ji}I_{ji}}$ is the relationship matrix between virtual points and source points obtained by MLS approximation.

Based on Eqs. (22)-(24), the unknown traction in Eq. (21) can be eliminated. Then a system of linear equations concerning unknown interfacial displacements is given by

$$\begin{bmatrix} \mathbf{A}_{kl}^{s_{I_{ij}}s_{I_{ij}}} & \cdots & \mathbf{A}_{kl}^{s_{I_{ij}}s_{I_{N-1N}}} \\ \vdots & & \vdots \\ \mathbf{A}_{kl}^{s_{I_{N-1N}}s_{I_{ij}}} & \cdots & \mathbf{A}_{kl}^{s_{I_{N-1N}}s_{I_{N-1N}}} \end{bmatrix} \begin{Bmatrix} \widehat{\mathbf{u}}_l^{s_{I_{ij}}} \\ \vdots \\ \widehat{\mathbf{u}}_l^{s_{I_{N-1N}}} \end{Bmatrix} = \begin{Bmatrix} \widehat{\mathbf{b}}_k^{s_{I_{ij}}} \\ \vdots \\ \widehat{\mathbf{b}}_k^{s_{I_{N-1N}}} \end{Bmatrix}, \tag{25}$$

where

$$\begin{Bmatrix} \mathrm{b}_k^{s_{I_{ij}}} \\ \vdots \\ \mathrm{b}_k^{s_{I_{N-1N}}} \end{Bmatrix} = \begin{Bmatrix} \mathrm{b}_k^{s_{I_{ij}}} + \mathbf{F}^{ss}_{I_{ij}I_{ji}} \mathrm{b}_k^{s_{I_{ji}}} \\ \vdots \\ \mathrm{b}_k^{s_{I_{N-1N}}} + \mathbf{F}^{ss}_{I_{N-1N}I_{NN-1}} \mathrm{b}_k^{s_{I_{NN-1}}} \end{Bmatrix}. \tag{26}$$

Hereafter, symbol M_i denotes the master interface (i.e. I_{ij},$(i<j)$) in domain Ω_i, and S_j denotes the slave interface (i.e. I_{ji},$(i<j)$) in domain Ω_j. The assembly of the interfacial coefficient matrix follows the rules below

rule1: when Ω_i=Ω_j and M_i=M_j

$$\mathbf{A}_{kl}^{s_{M_i}s_{M_j}} = \mathbf{A}_{kl}^{s_{M_i}s_{M_j}} + \mathbf{F}^{ss}_{M_iS_i} \mathbf{A}_{kl}^{s_{S_i}s_{S_j}} \mathbf{F}^{ss}_{S_jM_j}, \tag{27}$$

rule2: when $\Omega_i \neq \Omega_j$

i) M_i, M_j belong to the same subdomain

$$\mathbf{A}_{kl}^{s_{M_i}s_{M_j}} = \widehat{\mathbf{A}}_{kl}^{s_{M_i}s_{M_j}}, \tag{28}$$

ii) M_i, S_j belong to the same subdomain

$$\mathbf{A}_{kl}^{s_{M_i}s_{M_j}} = \widehat{\mathbf{A}}_{kl}^{s_{M_i}s_{S_j}} \mathbf{F}^{ss}_{S_jM_j}, \tag{29}$$

iii) S_i, M_j belong to the same subdomain

$$\mathbf{A}_{kl}^{s_{M_i}s_{M_j}} = \mathbf{F}^{ss}_{M_iS_i} \widehat{\mathbf{A}}_{kl}^{s_{S_i}s_{M_j}}, \tag{30}$$

iv) S_i, S_j belong to the same subdomain

$$\mathbf{A}_{kl}^{s_{M_i}s_{M_j}} = \mathbf{F}^{ss}_{M_iS_i} \widehat{\mathbf{A}}_{kl}^{s_{S_i}s_{S_j}} \mathbf{F}^{ss}_{S_jM_j}, \tag{31}$$

if there are no interfaces between two subdomains, the relevant parts are zero blocks in the interface coefficient matrix.

4. Numerical examples

Our research achievement in 3D elasticity multi-domain problems will be illustrated from different aspects in the following contents. The accuracy and convergence of the proposed method will be validated by the quadratic and cube polynomial solution, and the real-life examples will demonstrate the excellent performance of the new method in dealing with structures with thin or small feature sizes.

Error estimation and convergence are measured by the formula:

$$error = \frac{1}{|v^{(e)}|_{\max}} \sqrt{\frac{1}{M} \sum_{i=1}^{M} \left[v_i^{(e)} - v_i^{(n)} \right]^2}, \tag{32}$$

where $|v^{(e)}|_{\max}$ is the maximum value of the exact displacement u or traction t over M sample points, and superscripts e and n denote the exact and numerical solutions, respectively.

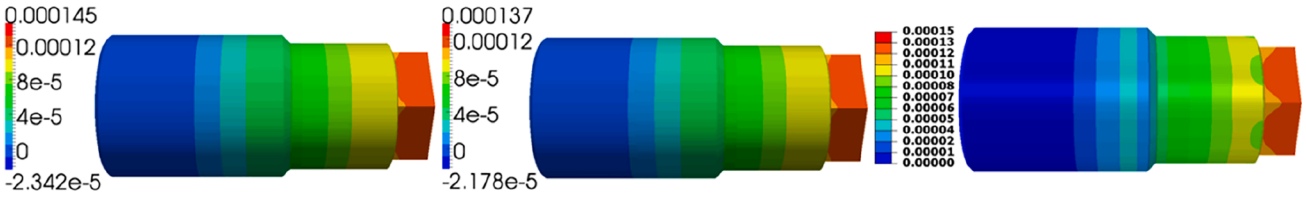

Fig. 19. Contour plots for displacement (a) single-domain DiBFM with 13,416 source nodes, (b) multi-domain DiBFM with 13,614 source nodes, and (c) FEM with 825,148 nodes.

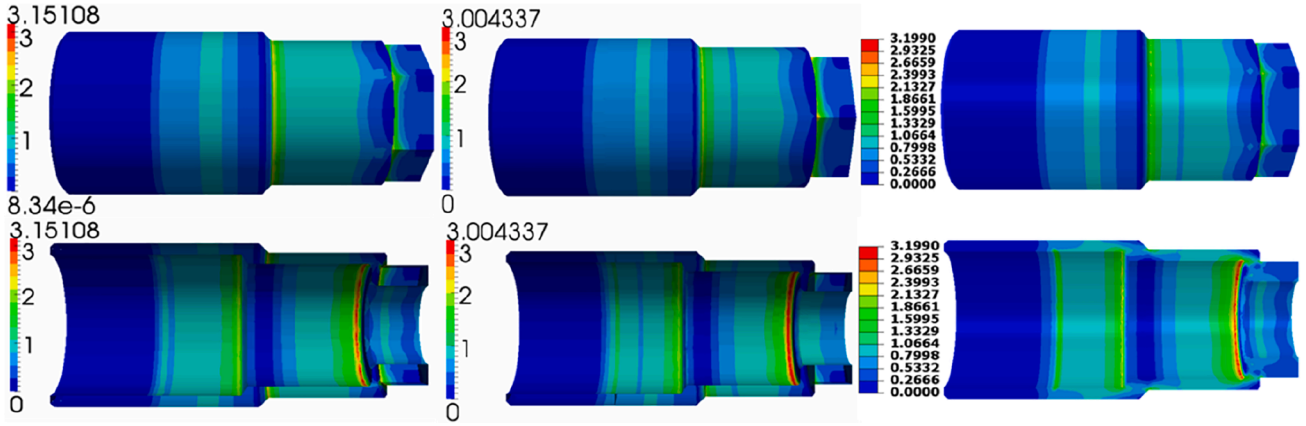

Fig. 20. Contour plots for Von-Mises (a) single-domain DiBFM with 13,416 source nodes, (b) multi-domain DiBFM with 13,614 source nodes, and (c) FEM with 825,148 nodes.

Unless otherwise mentioned,$\bar{t}$and$\bar{u}$represent the prescribed traction and displacement in the following examples. "*Err_Mises*," and "*time*" denote the relative errors for Von-Mises stress and CPU time. "*Max_Mises*" is the max Von-Mises stress. "*NE*," "*NS*," and "*NN*" represent the number of elements, source points, and nodes of FEM. "*DiBFM*," "*Multi-DiBFM*," and "*FEM*" in figures represent the single-domain method, multi-domain method, and FEM, respectively.

4.1. Bar

In order to demonstrate the accuracy and convergence of the proposed method, a bar with 5 subdomains (see Fig. 4(b)) is tested in a quadratic analytical field problem. The geometric dimension is shown in Fig. 4(a). Displacement boundary condition (see Eq. (33) is specified on all boundary faces besides the interfaces. The analytical solution is given by:

$$\begin{cases} U_1 = -2x_1^2 + 3x_2^2 + 3x_3^2 \\ U_2 = 3x_1^2 - 2x_2^2 + 3x_3^2 \\ U_3 = 3x_1^2 + 3x_2^2 - 2x_3^2 \end{cases}. \tag{33}$$

In this example, a node-to-element mapping scheme is implemented to build the relationship of the physical variables between the interface pair. The plane strain case with Young's modulus $E = 1.0Mpa$and Poisson's ratio ν=0.25 is considered here. The dual interpolation constant element is used to approximate the physical variables. The relative errors of Von-Mises stress calculated by multi-domain DiBFM and single-domain DiBFM are listed in Table 1; from this table, we can note that the numerical results by two methods convergence towards exact solution gradually with the increasing number of source points and the accuracy of the new multi-domain method can be guaranteed as well. A comparison of the computational efficiency between the multi-domain DiBFM and the single-domain DiBFM is shown in Fig. 5; the line chart demonstrates that our method is more efficient than the single one. The graphic in Fig. 6 depicts the distribution of the Von-Mises stress along with line AB when using the single-domain DiBFM with 10,736 source nodes and the multi-domain DiBFM with 12,000 source nodes; it indicates that both numerical results have a good agreement with the exact solution. The obtained numerical results in this example give a sufficient illustration of the accuracy and convergence of the proposed multi-domain algorithm.

4.2. Thin plate

To study the ability of the proposed method in coping with structures with thin walls, and testify the accuracy and convergence of our algorithm in solving the high-order analytical field problem, a thin plate subdivided into 9 subdomains (see Fig. 7(b)) is employed in this example. The geometric parameters are shown in Fig. 7(a), and the width-to-thickness ratio of this structure is just about 1.1%.

Dirichlet boundary conditions are imposed on the outer surfaces except the interface. The high-order analytical solution is given by:

$$\begin{cases} U_1 = x_2^3 - x_3^3 - 3(x_2 - x_3)x_1^2 \\ U_2 = x_3^3 - x_1^3 - 3(x_3 - x_1)x_2^2 \\ U_3 = x_1^3 - x_2^3 - 3(x_1 - x_2)x_3^2 \end{cases}, \tag{34}$$

Young's modulus $E = 1.0Mpa$and Poisson's ratio ν=0.25 are defined for the plane strain problem, assuming that the material is continuous and isotropic for all subdomains. The node-to-element mapping scheme is adopted once again. The dual interpolation constant element is employed in the discretization of the BIE.

The relative errors and CPU time obtained by the single-domain method and the multi-domain method are listed in Table 2, and the contrast of the computational efficiency is shown in Fig. 8; the information above denotes that the numerical results tend to be exact solution gradually with the increasing number of source points. Although the accuracy of the new method is a little lower than the single one, the convergence is still satisfied. Fig. 9 gives the comparison of the Von-Mises stress, calculated by multi-domain DiBFM with 10,722 source

points and the single-domain DiBFM with 10,722 source points, with the exact solution along with line AB. Those charts provide more proof for the accuracy of the addressed algorithm. From the given results, we can conclude that the current approach is available in geometric structures with thin walls and can ensure accuracy and convergence in simulating higher-order analytical field problems.

4.3. Cantilever slab

To investigate the capability of our multi-domain method in dealing with the real-life problem, a cantilever slab subdivided into 4 subdomains (see Fig. 10(b)) is employed in this section. The geometric size can be seen in Fig. 10(a). The displacement boundary condition $\overline{u}_i = 0, (i = 1, 2, 3)$ is imposed on the left-hand face of the block, and the traction boundary condition $P = 1.0\ Mpa$ is prescribed on the cantilever end, which can be seen in Fig. 10(c). Plane strain case with Young's modulus $E = 2.0\text{E}10^5 Mpa$ and Poisson's ratio ν=0.25 is assumed here, and the dual interpolation constant element is adopted as well.

A control group including the single-domain DiBFM method, the multi-domain DiBFM method, and the FEM is set to illustrate the convergence and the efficiency of our method, as in Table 3. Apparently, our method is convergent with the increasing number of source points, and it takes less time than the single-domain DiBFM. Simultaneously, this feature on time-saving can also be reflected through the line chart in Fig. 11; thus, the computational efficiency of our method is remarkable. The numerical results of the Von-Mises stress along with line AB, calculated by the single-domain DiBFM with 14,706 source nodes, the multi-domain DiBFM with 14,973 source nodes, and FEM with 1075,194 nodes, are depicted in Fig. 12; apparently, there is a common tendency in stress distribution. Figs. 13 and 14 plot the numerical results for displacement and Von-Mises stress by the three methods mentioned above. The difference of the max Von-Mises between our method and FEM is just 0.4%, and the stress concentration in the small feature size can also be simulated perfectly; therefore, the reliability and excellent performance of our multi-domain algorithm can be demonstrated.

4.4. Nozzle cap nut

For more convincing evidence on the robustness of our software package in solving complicated structures, a nozzle cap nut with 4 subdomains (see Fig. 15(a) and (b)) is used for the checking purpose in this example. The geometric size is dimensioned in Fig. 15(c). The assignment of the displacement and traction boundary condition can be seen in Fig. 16, in which the inner cylinder face is fixed, and the pressure $P = 1.0 Mpa$ acts on the interior of the nozzle cap nut. Plane strain case with Young's modulus $E = 2.0\text{E}10^5 Mpa$ and Poisson's ratio ν=0.25 is considered once again, and the dual interpolation constant element is used in the discrete process.

Numerical results of the Von-Mises stress and the CPU consumption, calculated by multi-domain DiBFM, single-domain DiBFM, and FEM, are recorded in Table 4. It is not difficult to find that the numerical results calculated by our multi-domain are convergent with the increasing number of source points, and the difference of the max Von-Mises between our method and FEM is just 3%. The Line chart in Fig. 17 reflects the contrast of the computational efficiency between the multi-domain DiBFM and the single-domain DiBFM. This figure can demonstrate that our method is capable of promoting computational efficiency in solving complicated structures. Fig. 18 gives the value of the Von-Mises stress along with line AB when using the single-domain DiBFM with 13,416 source nodes, the multi-domain DiBFM with 13,614 source nodes, and FEM with 825,148 nodes. The counterplot in Figs. 19 and 20 shows the distribution of displacement and Von-Mises stress, and they further demonstrate the reliability and robustness of our multi-domain algorithm.

5. Conclusions and discussions

In this paper, the DiBFM-HMLS combines with the matrix condensation technique to derive multi-domain formulas. Since the introduction of the DiBFM-HMLS, it is unnecessary to resort to other tools to cope with corner problems in each subdomain. A point-to-element interpolation has been constructed by MLS instead of the conventional node-to-node one. This mapping scheme provides convenience for free meshing in the interface groups. The assembly rules of the overall coefficient matrix concerning interfacial unknowns have been summarized as general cases according to the location of the subdomain. The multi-domain DiBFM-HMLS is more prominent in computational efficiency than the single-domain DiBFM-HMLS due to the blocked-sparse and the banded interfacial coefficient matrix. Numerical examples with the short edge or small chamfers have been given to illustrate these superiorities of the multi-domain DiBFM-HMLS.

Due to lacking of fast algorithm, the CPU consumption is also a challenge for current method to deal with large-scale problems (e.g. million degrees of freedom). Simultaneously, parallel computing is an existing issue for the multi-domain DiBFM-HMLS in the integral and mesh division. In future work, we will develop this method by supplementing the fast algorithm and parallel computing algorithm for contact problems, and the goal will come true soon. Another implementation of the demonstrated method to the 3D multi-domain contact problem is in progress.

Declaration of Competing Interest

On behalf of all authors, the corresponding author states that there is no conflict of interest.

Acknowledgments

This work was supported by National Natural Science Foundation of China under grant numbers 11772125 and 11972010.

References

[1] Zhang Jianming. Multidomain thermal simulation of CNT composites by hybrid BNM. Numer Heat Transf Part B 2008;53(3):246–58.
[2] Rodriguez RQ, et al. Fast BEM multi-domain approach for the elastostatic analysis of short fibre composites. Eur J Comput Mech 2017;26(5–6):525–40.
[3] Yue Q, Zhou W, Wang Q, Feng YT, Ma G, Chang XL. An adaptive phase-field model based on bilinear elements for tensile-compressive-shear fracture. Comput Math Appl 2022;105:112–35.
[4] Davì Giuseppe, Milazzo Alberto. Multidomain boundary integral formulation for piezoelectric materials fracture mechanics. Int J Solids Struct 2001;38(40–41):7065–78.
[5] Chen Tianzhi, et al. A symmetric Galerkin multi-zone boundary element method for cohesive crack growth. Eng Fract Mech 1999;63(5):591–609.
[6] Layton JB, et al. A symmetric Galerkin multi-zone boundary element formulation. Int J Numer Methods Eng 1997;40(16):2913–31.
[7] Kallivokas Loukas F, Juneja Tanjeet, Bielak Jacobo. A symmetric Galerkin BEM variational framework for multi-domain interface problems. Comput Methods Appl Mech Eng 2005;194(34–35):3607–36.
[8] Langer U, Of G, Steinbach O, et al. Inexact fast multipole boundary element tearing and interconnecting methods. Domain decomposition methods in science and engineering XVI. Berlin, Heidelberg: Springer; 2007. p. 405–12.
[9] Of, Günther, and Olaf Steinbach. "The all-floating boundary element tearing and interconnecting method." (2009): 277–98.
[10] Huang S, Liu YJ. A new simple multidomain fast multipole boundary element method. Comput Mech 2016;58(3):533–48.
[11] Zhang Jianming, et al. FMM-accelerated hybrid boundary node method for multi-domain problems. Eng Anal Bound Elem 2010;34(5):433–9.
[12] Ramšak Matjaž, Škerget Leopold. 3D multidomain BEM for solving the Laplace equation. Eng Anal Bound Elem 2007;31(6):528–38.
[13] Ramšak Matjaž, Škerget Leopold. A multidomain boundary element method for two equation turbulence models. Eng Anal Bound Elem 2005;29(12):1086–103.
[14] Wang Q, Feng YT, Zhou W, Cheng YG, Ma G. A phase-field model for mixed-mode fracture based on a unified tensile fracture criterion. Comput Methods Appl Mech Eng 2020;370:113270.
[15] Gao Xiao-Wei, Guo L, Zhang Ch. Three-step multi-domain BEM solver for nonhomogeneous material problems. Eng Anal Bound Elem 2007;31(12):965–73.

[16] Peng Hai-Feng, et al. Three-step multi-domain BEM for solving transient multi-media heat conduction problems. Eng Anal Bound Elem 2013;37(11):1545–55.
[17] Zheng Yong-Tong, et al. The coupled method of multi-domain BEM and element differential method for solving multi-scale problems. Eng Anal Bound Elem 2020; 113:145–55.
[18] Zhang JM, Lin WC, Dong YQ, et al. A double-layer interpolation method for BIE implementation for potential problems. Appl Math Model 2017;51:250–69.
[19] Zhang J, Lin W, Dong Y. A dual interpolation boundary face method for elasticity problems. Eur J Mech A Solids 2019;73:500–11.
[20] Zhang J, Chi B, Lin W, et al. A dual interpolation boundary face method for three-dimensional potential problems. Int J Heat Mass Transf 2019;140:862–76.
[21] Zhang JM, He R, Chi BT, et al. A dual interpolation boundary face method with Hermite-type approximation for potential problems. Appl Math Model 2020;81: 457–72.
[22] Zhang Jianming, He Rui, Lin Weicheng, Le Yang Baotao Chi, Suliman Chuanming Ju. A dual interpolation boundary face method with Hermite-type approximation for elasticity problems. Eur J Mech/A Solids 2020;82:104005.
[23] Liu Y. Fast multipole boundary element method: theory and applications in engineering. Cambridge University Press; 2009.